ilmedia

Technische Universität Ilmenau

Solomitckii, Dmitrii; Heino, Mikko; Buddappagari, Sreehari; Hein, Matthias;
Valkama, Mikko

Radar scheme with raised reflector for NLOS vehicle detection

Radar Scheme With Raised Reflector for NLOS Vehicle Detection

Dmitrii Solomitckii![ORCID], Mikko Heino![ORCID], *Member, IEEE*, Sreehari Buddappagari,
Matthias A. Hein![ORCID], *Senior Member, IEEE*, and Mikko Valkama![ORCID], *Senior Member, IEEE*

Abstract—The employment of passive reflectors enables the millimeter-wave automotive radars to detect an approaching vehicle in non-line-of-sight conditions. In this paper, the installation of such reflectors above the sidewalk at an intersection is proposed and studied, avoiding pedestrians' blockage and road dust effect at ground level. Through the analysis of the backscattering power, it is shown that the suggested scheme may detect an approaching vehicle in the blind zone at distances of $30\ldots50$ m to the intersection point. Additionally, the analysis shows that efficient operation is highly dependent on the spatial orientation and size of the reflector. Even a few degrees rotation may change the detecting range by several meters. In turn, the larger area of the reflector may cover longer detecting distances, improving the radar scheme's overall performance. It is also shown that further performance enhancement can be achieved by employing a C-type radar, contributing an extra 5 dB to the backscattering power relative to an A-type radar. However, despite these improvements, the strongest scattering centre of the detectable vehicle is systematically identified to the bumper zone.

Index Terms—Radar cross section, passive reflecting surface, physical optics, millimeter-wave radar, road vehicle, non-line-of-sight.

I. INTRODUCTION

MILLIMETER-WAVE (mmWave) automotive radars have become an essential part of the modern adaptive cruise control systems (ACCs), a decades-old feature that maintains a safe distance between driving vehicles. Recently, new types of radars operating at $76\ldots81$ GHz bands [1] for the front and corner applications have been gradually introduced to enhance safety and self-driving capabilities of vehicles. Additionally, fusion of radio-based and optical sensors is of increasing interest [2]. However, all the established
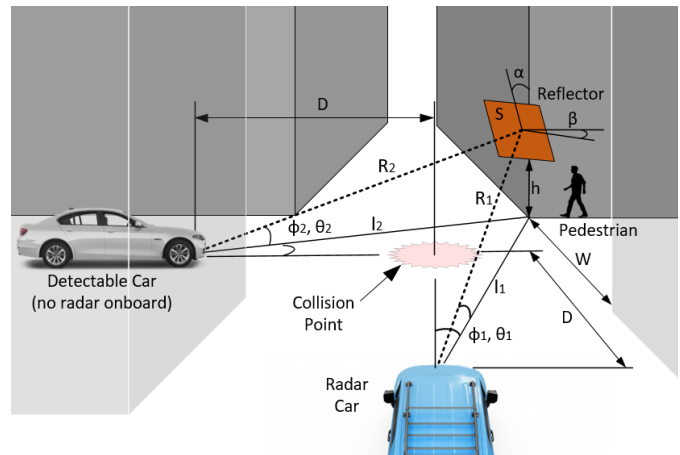
Fig. 1. Illustration of the radar scheme and operation in non-line-of-sight with passive reflector raised above the ground. The dotted line shows the backscattering signal path.

and more recent modern sensing systems require essentially a line-of-sight (LOS) channel between the sensor and the detectable object/vehicle.

Recently, in [3], the utilization of passive on-ground reflectors was proposed and validated by measurements for the early-stage detection of a vehicle driving around the corner in the non-line-of-sight (NLOS) conditions. Along this work, it was discovered that the ground-based location of the reflectors in the sidewalk interferes with pedestrians, who may block the reflections and, as a result, entirely disable the operation of the NLOS radar. Additionally, ground dirt adhering to the reflector's surface may deteriorate its reflectivity. Thus, in this paper, raising the reflector above the ground (see Fig. 1) to minimize the negative impacts is conceptually proposed while also thoroughly investigating the corresponding vehicle detection capabilities and performance through modelling. Specifically, the *backscattering power* of the radar signal, propagating along the dashed-line path in Fig. 1, is calculated with the developed ray-tracing (RT) tool and commercial electromagnetic (EM) simulator, in order obtain accurate and reliable results.

In the existing literature, analyzing the backscattering properties of different vehicles at mmWave frequencies is a relatively popular topic, with the radar cross-section (RCS) being the primary metric. To this end, the authors in [4] proposed a reliable methodology for measuring small and large targets at

the W-band. As a part of this, the backscattering behaviour and RCS of a small car model were studied. The authors in [5], in turn, measured the RCS of a sedan car at the 77 GHz frequency band employing H- and V- polarizations. Furthermore, the authors in [6] simulated and measured K-band scattering data of a civilian vehicle. All these works mostly focus on vehicles' backscattering properties and do not study any specific radar schemes or radar applications. Additionally, the height of the reflector h in Fig. 1 and the RCS of the detectable car become effectively dependent on the elevation angle θ_2 – an issue that has not been addressed in the existing literature.

Additionally, there are many works dealing with co-channel interference – one of the primary limiting factors in automotive radar applications [7]. In this regard, the authors in [8]–[10] seek to identify and suppress the interference by neural networks. Meanwhile, authors in [11]–[13] utilize more conventional signal processing approaches to improve the radar detection capabilities under interference. However, the NLOS radar scheme with raised reflector has not been studied in this context either.

The contributions of this article with respect to the existing literature can be shortly stated and summarized as follows:

1) The accurate RCS of a detectable car is modelled as a function of azimuth and elevation angles. The strongest scattering centre on the detectable car body is also identified.
2) Analysis of the backscattering power in the proposed NLOS radar scheme as a function of radar type and spatial orientation of reflector is carried out. Additionally, the optimal configuration of the scheme is determined.

Additionally, the co-channel interference issue is noted and highlighted establishing an important topic for future work.

The rest of the paper is organized as follows. Section II describes the considered NLOS vehicle detection scenario and the detectable car models. Next, Section III explains the EM methodology for the RCS modelling and the calculation of the backscattering power. In Section IV, first, the RCS of the simplified car model is determined to investigate the basic relationship between scattering and geometry. Then, accurate RCS simulations of the detectable car model are performed. After this, the precise RCS data is employed to calculate the backscattering power in Section V. Additionally, the elementary evaluation of the co-channel interference as one of the limiting factors is noted and pursued. Finally, conclusions are given in Section VI.

II. SCENARIO AND DETECTABLE CAR MODELS

Three dimensional (3D) computer-aided design (CAD) models of the NLOS vehicle detection scenario and the detectable car are needed in order to calculate the radar scheme's backscattering power. Detailed information about each of these elements is presented below.

A. 3D Model of Scenario

The topology of the virtual 3D CAD scenario is similar to the one shown in Fig. 1. It is designed to calculate the

TABLE I
SCENARIO PARAMETERS

Dimension	Value/Range	Notes
D [m]	10 ... 50	Distance to the collision point
α [°]	6, 8, 12	Orienting elevation angle of the reflector
β [°]	45	Orienting azimuth angle of the reflector
h [m]	2.0	Rising height
W [m]	8.0	Road width
S [m^2]	1.0, 1.3	Reflector's area

backscattering power of the radar scheme with raised reflector in a typical urban blind intersection. Similarly to Fig. 1, it consists of four cubical buildings surrounding the intersection and a flat square reflector, rising above the road pavement and fixing on the building corner. The geometrical parameters of the scenario are summarized in Table I. The radar car is replaced with a route of collocated transmitting (Tx) and receiving (Rx) antennas, while a point scatterer represents the detectable vehicle with assigned monostatic RCS from the accurate 3D CAD model of the detectable car.

B. Accurate 3D Model of Detectable Car

An accurate 3D CAD model of the detectable car is needed to calculate the real RCS for the backscattering power evaluations. The model represents a detailed virtual copy of an existing real-world car. It should satisfy a number of requirements in order to carry out accurate EM evaluations. First, the CAD-model should be geometrically precise, which can be preliminarily recognized through the size of a CAD-file (rule of thumb typ. 30-50 MB) as well as density/quality of the mesh grid. Specifically, the "proper density" means that the CAD-model should have a smooth mesh-grid without sharp stitches, and the "good quality" means that most of the facets should have the form close to an equilateral triangle (lowest aspect ratio). Secondly, the selected 3D CAD-model should represent an assembly (*.asm) of separate solid parts to which various materials might be assigned. Thirdly, a real-world prototype of the virtual 3D model must have already completed measurements of RCS. Matching the measured results with the simulated results demonstrates the geometric accuracy of the selected 3D model and methodology.

All the above-mentioned selection criteria are realized in the 3D CAD-model of Mercedes E-class (W213), available through [14]. It is a classic sedan with a very typical geometry. The CAD-model has an adaptive mesh grid to emphasize small details and a good aspect ratio of all facets. Additionally, the model was assembled from separate solid components such as ring disks, glass parts, headlights etc. Finally, the real-world prototype of this car is measured in [5], the results of which are utilized in the calibration of the applied EM methodology and validation of the CAD-model's accuracy.

The car measurements were conducted in an automotive antenna test facility: virtual road simulation and test area (VISTA) at the Technische Universität Ilmenau in Thuringia, Germany. It is a semi-anechoic shielded chamber with dimensions of 6 x 12 x 9 m and equipped with a turntable of diameter 6.5 m. Automated measurements were

TABLE II
GEOMETRICAL PROPERTIES OF THE SIMPLIFIED MODELS

Surface	Orient. angle* [°]			Area [m²]			Curvature [m]		
	#1	#2	#3	#1	#2	#3	#1	#2	#3
Roof	90	90	90	4.56	3.99	3.82	0	0	0
Roof edge	63.5	63.5	70.0	0.13	0.13	0.13	0	0	0
Windshield	26.6	45.0	26.6	1.27	1.61	1.61	0	0	10
Hood	82.0	82.0	82.0	0.64	0.64	0.64	0	0	0
Radiator	25.0	25.0	25.0	0.64	0.64	0.64	0	0	0
Bumper	0	0	0	0.63	0.63	0.63	0	0	0

* Orientation angle γ is the angle between the surface's normal and the ground plane at $\phi = 0°$.

conducted to record coherent data by controlling the VNA and the turntable, respectively, with a computer program. The instrumentation radar is a vector network analyser (VNA) equipped with millimetre-wave extension modules connected to pyramidal horn antennas in a quasi-monostatic configuration. The measurement system is computer-controlled with the results recorded by rotating the turntable in 1° increments, holding it at that aspect angle and sweeping the VNA from 76 … 81 GHz. This is a standard recommended procedure called index-and-stop measurement approach that offers more accuracy than measurements at continuous slow motion. The device-under-test is placed at the centre of the turntable and rotated in the clockwise direction with steps of 1° to span the entire range of azimuth angles from 0° to 360°. The measured data represents a collection of complex scattering parameters S_{21} for a particular frequency and azimuth angle. In order to derive accurate and absolute RCS values from this measured data, a comprehensive post-processing technique described in [5] was applied in frequency and time–domain. Initially, background subtraction in the frequency domain is used to eliminate components of the data that are unchanged by introducing the target into the measurement range. Subsequently, range gating is performed in the time-domain using a Kaiser window function to eliminate the target neighbourhood's contributions. The co-polarisation components were measured to include comprehensive coverage of the relevant radar types, namely HH and VV. A detailed description of the data acquisition, post-processing technique and results can be found in a separate publication [5].

C. Simplified 3D Models of Detectable Car

In this work, also simplified 3D CAD models of the detectable car are pursued and utilized, in order to discover and understand the essential relationships between the backscattering and the system geometry. An example of the simplified 3D model is shown in the corner of Fig. 3. It consists of six surfaces whose spatial orientation is specified by γ. More detailed information is given in Table II.

To this end, three simplified car models with different geometry of the windshield are considered. Specifically, Model #2 has the slope of 45.0°, while the slope of Model #1 and #3 is 26.6°. At the same time, Model #3 has a rounded windshield with 10 m radius, while the windshields of Models #1 and #2 are entirely flat. In addition to geometry, two electrically different types of windshields are considered. The first one

represents a typical dielectric windshield made of glass. The second one is an athermic windshield covered by a thin metal oxide film which partially blocks harmful solar irradiation. Comparison between windshields made of different materials will provide useful information about the losses associated with the dielectrics.

III. UTILIZED EM METHODOLOGY

The EM methodology builds on the radar range equation (RRE), calculating the proposed radar scheme's backscattering power. However, the components of this equation should be preliminarily parametrized numerically. In the next subsections, the correspondings procedures are explained.

A. Backscattering Power

According to ITU-R recommendations in [1], the RRE is selected as a basis for calculating the backscattering power, P_r, in the considered automotive radar application. To this end, based on the considered deployment, the RRE reads

$$P_r = \frac{P_t \lambda^2 \sigma}{(4\pi)^3 (R_1 + R_2)^4} G_t G_r G_{proc}, \tag{1}$$

where λ denotes the wavelength, R_1 and R_2 are the lengths of Tx-to-reflector and reflector-to-target paths, while σ is monostatic RCS of the detectable car. Finally, G_t and G_r are the Tx and Rx antenna gains, whose calculation methodology is explained in [1]. Specifically, as noted in [1], the antenna radiation patterns of Tx and Rx can be approximated through the following empirical expressions of the form

$$G(x) = \begin{cases} G_0 - 12x^2 & 0 \le x \le 1.152 \\ G_0 - 15 - 15\log(x) & 1.152 \le x. \end{cases} \tag{2}$$

In (2), $x = \Psi/\Psi_\alpha$, where Ψ and Ψ_α are given by

$$\Psi = \arccos(\cos\phi_1 \cdot \cos\theta_1) \tag{3}$$

and

$$\Psi_\alpha = \frac{1}{\sqrt{(\frac{\cos\alpha}{\phi_{3dB}})^2 + (\frac{\sin\alpha}{\theta_{3dB}})^2}}, \tag{4}$$

with $\alpha = \arctan(\frac{\tan\theta_1}{\sin\phi_1})$. In above, G_0 is the maximum gain in near horizontal plane, expressed in dBi, θ_1 and ϕ_1 are absolute values of the elevation and azimuth angles, expressed in degrees and illustrated in Fig. 1, while θ_{3dB} and ϕ_{3dB} are the 3 dB beamwidths in the vertical and horizontal planes, measured in degrees. In this paper, both A- and C-types of radar [1] are considered, whose properties are listed in Table III. As concrete visual examples, two antenna patterns are shown in Fig. 2. These types of radars were chosen due to their significant differences in both radiation patterns (see Fig. 2) and applications (AAC and side detection).

Finally, G_{proc} in (1) is the processing gain which, as shown in [3], is viable with any type of reflector in the considered scheme. In this paper, the OFDM-radar gain calculated as the

TABLE III
UTILIZED RADAR ANTENNA SYSTEM PROPERTIES

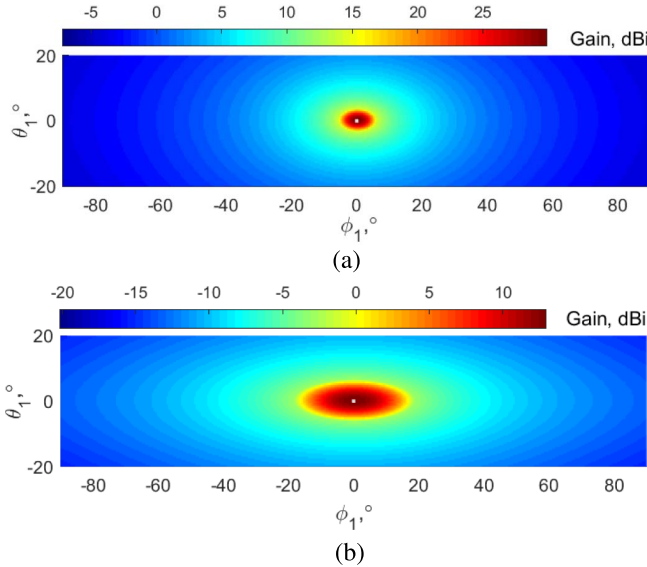| Radar	ϕ_{3dB}		θ_{3dB}		G_0		Ptx	Application
	Tx	Rx	Tx	Rx	Tx	Rx		
A	±5	±5	±3	±3	30	30	10	ACC
C	±12.5	±16	±5.5	±5.5	23	13	10	Corner

Fig. 2. Example illustrations of the antenna patterns, using equation (2), for a) A-type radar Rx, and b) C-type radar Tx.

$G_{proc} = 10 \log_{10}(S \cdot R) = 60 \, \text{dB}$ is applied, where S and R denote the number of subcarriers and OFDM-symbols.

The overall procedure for calculating the backscattering power P_r in the proposed radar scheme with raised reflector can be eventually summarized as follows:

1) First, monostatic $\sigma(\phi_2, \theta_2)$ of the accurate detectable car model is precalculated and stored.
2) Then an adapted version of the image-based RT tool utilized in [15] is employed to calculate the angles ϕ_1, θ_1, ϕ_2, θ_2 and the lengths of the paths R_1 and R_2 shown as dashed line in Fig. 1.
3) Then, $G_t(\phi_1, \theta_1)$ and $G_r(\phi_1, \theta_1)$ radar gains are calculated at estimated angles by formula (2).
4) Finally, the precalculated $\sigma(\phi_2, \theta_2)$, $G_t(\phi_1, \theta_1)$ and $G_r(\phi_1, \theta_1)$ are substituted into equation (1). The output metric is the backscattering power P_r as a function of D, spatial orientation of reflector, and the radar type.

It is also worth noting that the RRE is applied without including the reflector's bistatic RCS in it due to the following fundamental reasons. First, because the reflector size is very large compared to the wavelength (3 mm versus 1 m), it essentially acts as a perfect mirror and does not commit any losses to the backscattering signal. Second, taking into account that the basic RRE supports only point scatterers (the distance to the object should be much larger than the size of the object itself [16]), consideration of the passive reflector at small distances D may cause significant errors. Finally, there

are several practical challenges to calculate the bistatic RCS of the electrically large reflector, explained in Sub-section IV-C.

B. Simulation of RCS

As noted in [16], the general analytical expression of σ in (1) reads

$$\sigma = \lim_{r \to \infty} 4\pi r^2 \frac{|E^{scat}|^2}{|E^{inc}|^2}. \tag{5}$$

The E^{inc} in (5) denotes the amplitude of the incident plane wave, and E^{scat} indicates the scattered field created by surface currents. When the wavefront falls on a surface, it creates the current on it, which, in turn, produces a secondary back-scattering wavefront, propagating from the surface to the observation point. In case of a perfect electrical conductor (PEC), the surface current does not experience any attenuation. On the other hand, if the surface is resistive, the current decreases proportional to the surface impedance η, expressed as

$$\eta = \sqrt{\frac{j\omega\mu}{\sigma' + j\omega\epsilon}}\eta_0, \tag{6}$$

where ω is radial frequency, μ and ϵ are relative permeability and permittivity, σ' is conductivity, and, finally, $\eta_0 = 120\pi$ is free space impedance.

The EM modelling of σ in (1) is executed in Ansys HFSS, where the shooting and bouncing ray (SBR+) method with the uniform theory of diffraction (UTD) and physical optics (PO) are applied to calculate E^{inc} and E^{scat} in (5) [17]. They are the most appropriate techniques for electrically large objects when compared to full-wave methods. Possible attempts to simulate σ with the alternative full-wave FEM-IE method leads easily to the out of memory problems on high-performance (I7, 32 GB RAM) laptops. Although both methods are based on the calculation of surface currents, the full-wave methods (including FEM-IE) require ultra-high dense mesh (especially at small wavelength), which is computationally very expensive to solve and store. Therefore such techniques are best suited to small near-field problems. Alternatively, SBR+ does not require dense mesh, while the employment of beams in the large scale deployment reduces computational time. Additionally, according to [17], SBR+ supports dielectric materials. In this paper, the "impedance boundary condition" is applied to all dielectrics, while alternative boundary conditions called in HFSS as "finite conductivity" is only applicable for good conductors [18]. Practical materials such as metal, glass, and plastic (see Table IV) are assigned to different parts of the detectable car to obtain accurate simulation results. All the materials are paramagnetic, meaning $\mu = \mu_0$.

Substitution of values in Table IV into formula (6) brings $\eta = 150 \, \Omega$ for the glass windshield and $248 \, \Omega$ for the bumper. The thickness is essentially meaningless since HFSS SBR+ does not support any penetration into the material.

IV. RCS MODELING RESULTS

A. Monostatic RCS of Simplified Detectable Car Model

This subsection aims to find fundamental relationships between the backscattering and the geometry of the
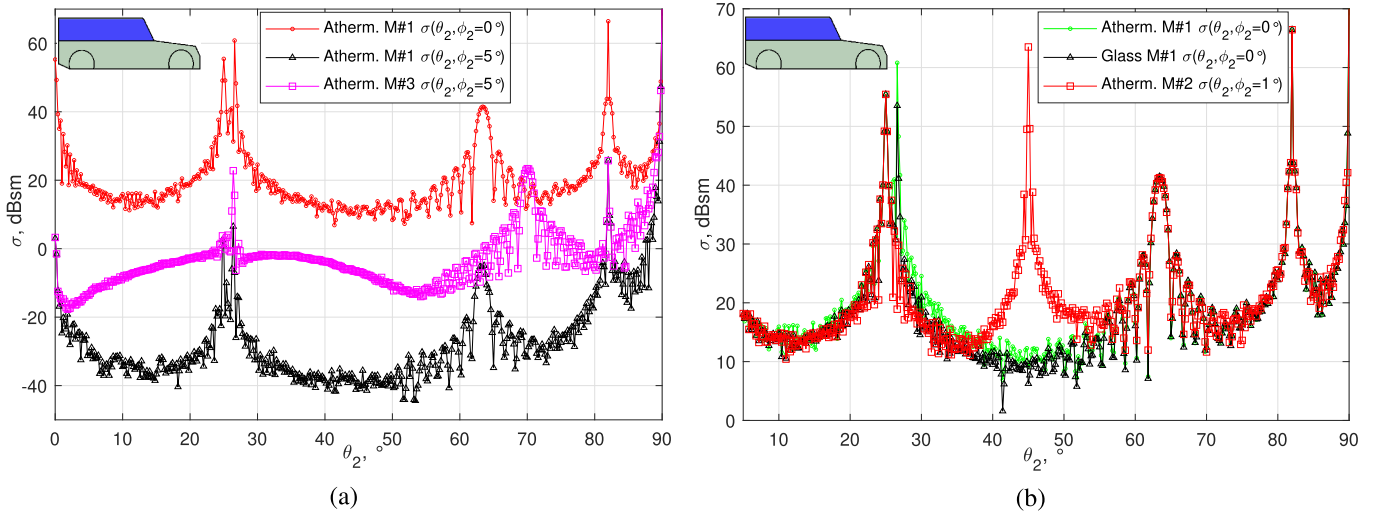
Fig. 3. In (a), the obtained values of σ for model #1 and model #3 with flat and curved windshields, respectively, are shown. In (b), the corresponding values of σ are illustrated for model #1 and model #2 with flat glass and flat athermic windshields, respectively.

TABLE IV
UTILIZED MATERIAL PROPERTIES AT 76 … 81 GHz

Part	Material	ϵ	σ, S/m	$tan(\delta)$	Ref.
Windshield	Typ.glass	6.27	0.70	0.029	[19]
	Metal. glass	1	10^{30}	0	HFSS DB
Body	PEC	1	10^{30}	0	HFSS DB
Bumper	Polymer	2.3	$42 \cdot 10^{-4}$	$2.3 \cdot 10^{-4}$	[20]

simplified car models introduced in Sub-section II-C. Such low-polygonal virtual vehicles are advantageous in this context since their surface orientations are strictly spatially predefined. Here, each of these models is illuminated by a $76 \ldots 81$ GHz plane wavefront, whose direction changes along the elevation angle $\theta_2 = 0 \ldots 90°$ at $\phi_2 = 0°$ and $5°$. The obtained results are shown in Fig. 3. Since the obtained raw data contains significant fluctuation, cross-frequency averaging in the range $76 \ldots 81$ GHz with 1 GHz step is performed. In practice, the backscattering signal, arriving at the Rx antenna from the detectable vehicle, is subject to the shape of these angular-dependent fluctuations, while their specific effect on, e.g., the radar detection probability depends on radar waveform and detection signal processing method.

The simulated results of Model #1 with the flat windshield are shown in Fig. 3(a). First, it can be noticed that at $\phi_2 = 0°$ (red curve) each of the Model #1 surfaces described in Table II creates an individual peak. Specifically, scattering occurs from the rooftop at $\theta_2 = 90°$, while the peak from the hood appears at $\theta_2 = 82°$. At $\theta_2 = 65°$, the rooftop edge starts to be visible as well. However, due to a small area of the latter (see Table II), it does not create a peak. The peaks in σ characterizing the scattering from the radiator grid and the bumper zone are located at $\theta_2 = 25°$ and $\theta_2 = 0°$ accordingly. The Model #1 has a scattering peak caused by the windshield at $\theta_2 = 26°$.

When the incident wavefront impinges on Model #1 at $\phi_2 = 5°$ (black line in Fig. 3(a)), the level of the overall

σ curve is some 40 dB lower compared to the red curve. Moreover, additional simulations show that even a few degree displacements of ϕ_2 can lead to 30 dB drop in the σ magnitude, though not shown explicitly in Fig. 3(a). On the other hand, Model #3 with the curved windshield shown in Fig. 3(a) (pink curve) has a smooth behaviour of σ around $\theta_2 = 25°$. This happens because the curved surface consists of a set of simple sub-planes reflecting signal at different angles. Additionally, the intersection of the incident flat wavefront and rounded surface occurs at an effective area smaller than the windshield area. Consequently, a smaller windshield radius causes a smaller contact area with the wavefront, leading to a smaller σ peak magnitude.

Next, the analysis of σ as a function of windshield slope is performed. For this purpose, the RCS comparison of Model #1 (green) and Model #2 (red) with athermic windshields is completed. The results are presented in Fig. 3(b). As expected, the peaks created by the two windshields with different slopes are located at $\theta_2 = 26°$ and $45°$. The obtained values of θ_2 are similar to the orientation angles listed in Table II for Model #1 and Model #2.

Next, Model #1 with athermic (green) and glass (black) windshields are compared in Fig. 3b. Based on this, it is seen that purely dielectric glass reduces the reflectivity by 3–6 dB compared to the athermic one. Such a surprisingly small difference can be explained as follows. The dominating reflection mechanism is specified by reflection coefficient, expressed as $\Gamma = (\eta - \eta_0)/(\eta + \eta_0)$, where surface impedance η is one of the two components. Following this, it can thus be stated that the difference should be in the order of Γ, varying in the above-mentioned range [15].

In summary, the following conclusions can be drawn and noted based on the obtained results. First, vehicles with smooth body geometry (e.g., sports cars) may scatter signals in a wide angle-range, increasing their detectability from different observation points. Oppositely, the cubical geometry (e.g., vans, trucks) creates more strong scattering to a particular direction
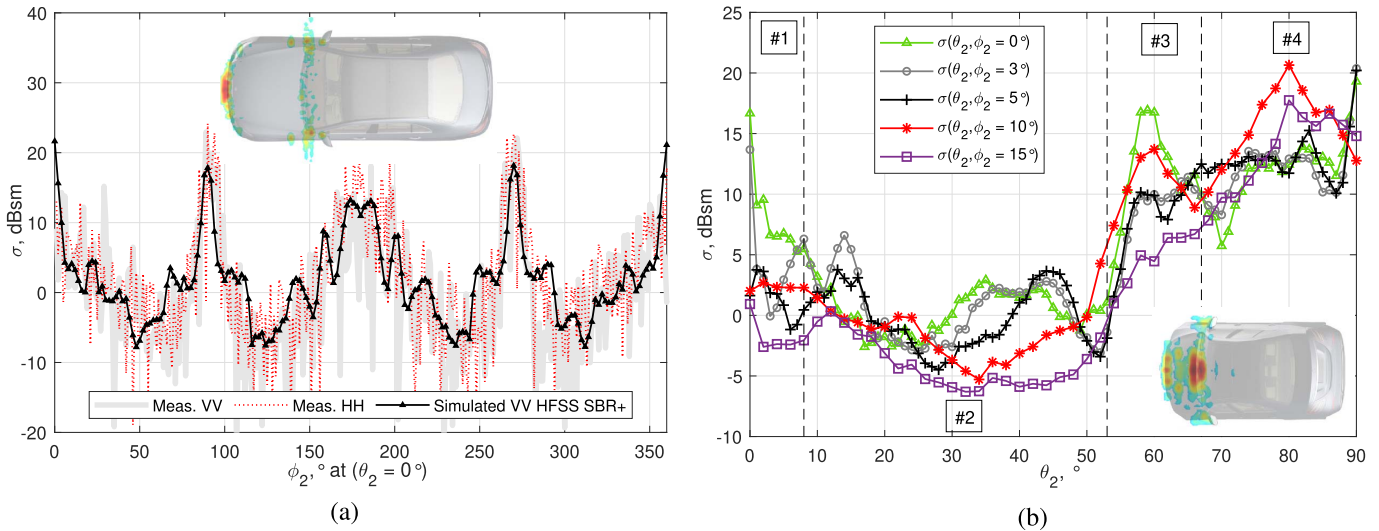
Fig. 4. The measured (solid gray and dotted red curves) as well as HFSS-simulated (black curve) $\sigma(\phi_2)$ values of Mercedes-Benz W213 are illustrated in (a). The simulated $\sigma(\phi_2, \theta_2)$ values of Mercedes-Benz W213 with glass and athermic windshields are shown in (b). Also inverse synthetic aperture radar (ISAR) images are illustrated.

in a very narrow angular range. Thus, the effective operation of the proposed radar scheme in such condition could be challenging. Finally, the metalized coatings on the windshields do not crucially increase backscattering as expected.

B. Monostatic RCS of Accurate Detectable Car Model

The calculation of an accurate value of the RCS σ in (1) consists of two parts. First, the comparison between the measured $\sigma(\phi_2)$ of the real Mercedes-Benz W213 and the simulated $\sigma(\phi_2)$ of the virtual model – described in Sub-section IV-B) – is completed to determine the precision of the selected SBR-based methodology and 3D CAD model of the detectable car. After this, in the next stage, the simulation of the $\sigma(\phi_2, \theta_2)$ of the virtual model is carried out.

During the modeling at the calibrating stage, the wavefront direction varies from $\phi_2 = 0$ to $360°$, at constant $\theta_2 = 0°$. Similarly to the simulation of the simplified detectable car model, the calculated σ is averaged across the $76 \ldots 81$ GHz band and additionally smoothed by a Savitzky-Golay filter with the averaging coefficient 3. The comparison of measured and simulated results are shown in Fig. 4(a), where four regions can be recognized. The scattering peaks from the front of Mercedes-Benz W213 occurs at $\phi_2 = 0°$, while the rear part scatters towards $\phi_2 = 180°$. Left and right sides of the car are visible through peaks at $\phi_2 = 90°$ and $270°$, accordingly. The obtained simulation results agree well with the measured ones, which justifies the selected 3D CAD model of Mercedes-Benz W213 and overall demonstrates the good accuracy of the methodology.

The next step is to calculate $\sigma(\phi_2, \theta_2)$ with the calibrated methodology. The results are presented in Fig. 4(b). The results can essentially be divided into four zones. The first Zone #1 is responsible for scattering from the front part of the car. In particular, the scattering from the license plate and bumper form the specular peaks, similar to the discussion in Sub-section IV-A. The inverse synthetic aperture radar (ISAR)

image, depicted also in Fig. 4(b), justifies this statement – the large red zone shows the strongest backscattering centre.

The next Zone #2 has the lowest σ magnitude due to obliquely oriented surfaces towards the incident wavefront. On the contrary, the Zone #4 has the highest σ magnitude due to the large areas of roof and hood surfaces. Nevertheless, both of these zones are not efficient in the proposed radar scheme.

The last Zone #3 demonstrates the backscattering phenomenon from the windshield, which can be very useful in the context of the suggested radar scheme. The values of σ in the zone, shown in Fig. 4(b) specify the strongest peak magnitude at $\theta_2 = 60°$ and $\phi_2 = 0°$. According to the ISAR image in the right bottom part of Fig. 4(b), this peak indeed corresponds to the scattering from the windshield, shown as a sizeable red zone.

Finally, according to Fig. 4b, it is seen that the higher values of ϕ_2 reduce the overall magnitude of $\sigma(\theta_2)$. This negative effect is highly noticeable in Zone #1, where the specular reflection from the number plate dominates.

In summary, based on the comprehensive analysis of $\sigma(\phi_2, \theta_2)$ behavior, the following averaged magnitudes can be determined for Mercedes-Benz W213 in different θ_2 regions. In Zone #1, the mean value of σ is 2 dBsm, with 3.4 dB standard deviation. In Zone #3, the mean magnitude and standard deviations are 10 dBsm and 3.1 dB, respectively. Depending on the θ_2, one of these values will be substituted in (1) during the calculation of the backscattering power in the next section. The other two zones are not properly oriented for the radar scheme and will thus not be considered.

C. Challenges Related to Reflector RCS Simulations

Including the reflector RCS in (1) could be thought to give an advantage in calculating the backscattering power with variable reflecting surfaces. However, Sub-section III-A already outlined some fundamental reasons why applying the reflector RCS in (1) can result to inaccuracies in RRE.
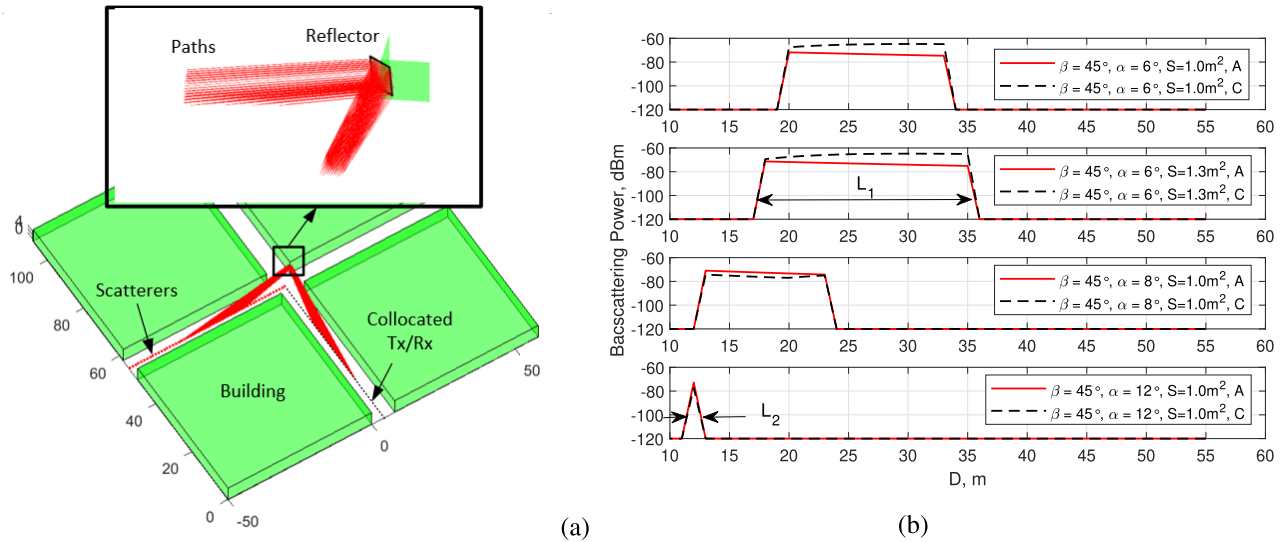
Fig. 5. Variation of ϕ_1 and θ_1 for different road widths (a), and the backscattering power as a function of environmental conditions (b).

Besides this, some practical challenges are also associated with straightforward EM modelling of reflector in the described radar scheme. First, by default, when the object size is much larger than the wavelength (more than ×1000 times in our case), the associated computations become extremely heavy and resource-hungry. Furthermore, the challenges further escalate through the bistatic nature of scattering itself, when each of the incident direction generates a particular RCS pattern. Nevertheless, the set of bistatic RCSs of a reflector can in principle be obtained in a reasonable time on a high-performance computing solution – something that the authors also pursued.

However, as soon as the collected RCS pattern was employed in (1), the authors faced a problem of non-sufficient angular discretization of the scattered field with dominating specular reflection. Specifically, based on Sub-section IV-A and Fig. 3, flat and electrically large surfaces backscatter the signal in the form of narrow peaks. Therefore, a dense distribution of receiving points is required to recognize them. Based on the modelling experiments that were carried out, even 1° discrete angular step turned out to be insufficient since still peak errors of about 20 dB were observed. Further densification of the receiving points turned out to be very challenging due to the exponential rise of the computational time as well as the very large amount of needed memory.

As a result, the authors finally decided to avoid deploying the bistatic RCS in (1), due to the high sensitivity of the results to the input settings and the related computational challenges. RCS results data are openly available at [21].

V. BACKSCATTERING POWER RESULTS

In this section, the backscattering power results as functions of the reflector area S, orientation (α, β) and the radar type (types A and C) are provided, through (1). The input parameters are listed in Tables I and III while σ is defined in Sub-section IV-B. Based on the analysis of the obtained results, suggestions for the design parameters for the reflector, i.e., the choices of α, β and S, are also provided.

Before proceeding to the numerical results, a comparison between the windshield and bumper backscattering (Zones #1 and #3 in Fig. 4) as a part of the proposed radar scheme is pursued. For this purpose, an equation linking θ_2 and h is shortly deduced, addressing how well the reflector and the windshield are aligned in the proposed radar scheme. To this end, the distance from the detectable vehicle to the building corner l_2 (see Fig. 1) can be expressed as $l_2 = \sqrt{(D + 0.5W)^2 + (0.5W)^2}$, while $h = l \tan(\theta_2)$. Then, the substitution of l_2 to h establishes the required relationship as $h(\theta_2) = \sqrt{(D + 0.5W)^2 + (0.5W)^2} \tan(\theta_2)$. Considering then that the windshield scattering peak appears at $\theta_2 = 60°$, the following comparative results can be obtained: $h = 120\,\text{m}$ at $D = 65\,\text{m}$ and $h = 10\,\text{m}$ at $D = 0\,\text{m}$. These outcomes show that the backscattering signal from the windshield would require unrealistically large value of h, and thus the Zone #3 will not be considered further in the following.

A. Scenario and Results

The considered deployment is shown in Fig. 5, mimicking the scenario depicted in Fig. 5(a). The corresponding obtained results are demonstrated in Fig. 5(b).

First, it can be seen that the variation of α affects the behaviour of signal propagation in the blind region in a very crucial manner, which, in turn, defines the detection efficiency specified by the duration of backscattering signal denoted as L. In this paper, the value of L quantifies the distance within which the car is detectable in the blind zone. The longest simulated value is $L_1 = 17\,\text{m}$ (second sub-figure in Fig. 5(b)), while the shortest one is $L_2 = 2\,\text{m}$ (fourth sub-figure in Fig. 5(b)). As an example, at a violating speed of 80 km/h, the detectable vehicle may pass the L_1 already in 0.8 seconds, which basically would deliver only eight measured samples to the radar-equipped vehicle assuming a 100 ms measurement cycle. The substantially shorter values of L_2 would already indicate very challenging measurement cycles below 10 ms.

Furthermore, based on the obtained results in Fig. 5(b), $\alpha = 6°$ at $\beta = 45°$ facilitates good and robust performance. It is also noted that the values of α cannot be made arbitrarily low due to the practical reasons. Firstly, at $\alpha < 6°$, the detection range would grow exponentially, leading to unpractical sensitivity. Additionally, at small values of α, the detection range would exceed the maximal range of $D = 50$ m in our scenario.

Stemming from the results in the first and second subfigures of Fig. 5(b), the size of the reflector also matters. Specifically, an additional 30 % to the reflector area leads to an increase of L_1 by an extra 2.5 m. In practice, the size of the reflector is, however, likely to be limited by the sidewalk width.

Finally, the type A and C radars show comparable backscattering power at $D < 20$ m while the type C radar can add an extra 5-10 dB gain at $D > 20$ m. The reason for this is the following. At small values of D, the backscattering power propagates through the main lobe in both radar types. On the contrary, at relatively large distances, due to the wider half-power beamwidth, the type C radar shows better performance than the type A radar.

Based on the obtained results, the following conclusion can be drawn. First, a feasible configuration of the proposed radar scheme has the following parameters in the considered scenario: $\alpha = 6°$, $\beta = 45°$, S $= 1.3$ m^2. Meanwhile, the type C radar facilitates somewhat higher (+5 dB) backscattering power compared to the type A radar.

B. Backscattering vs. Interference Power

In general, we note that one of the potential performance limiting factors for the automotive radars is co-channel interference, occurring when antennas illuminate each other with an interfering signal, especially if the interference power is comparable to the target signal power level. Therefore, the described radar scheme can be subject to relatively strong interference effects when the detectable vehicle is also equipped with an onboard radar, operating in the same frequency band. Moreover, following the paths depicted in Fig. 1, the observed power of the backscattering signal is likely to be lower than that of the other illuminator. Specifically, the propagation path of the interfering signal is twice shorter, and also the signal does not experience any losses on scattering.

Simplified evaluation of the interfering signal power with the basic Friis formula and backscattering power with the radar range equation will yield easily signal-to-interference ratios (SIRs) in the order of -30 dB. In such conditions, the successful operation of the proposed scheme can be challenging – however, it is also noted that this depends largely on the specific type of the radar and the related radar signal processing methods and the corresponding radar processing gain. Additionally, some interference mitigating techniques [7], [22] can help to further improve the radar scheme performance. In particular, spectral separation, scheduling, or polarisation diversity between interfering and backscattering signals may relax the interference issues. Further investigation of the interference issues and the different potential mitigation mechanisms are important topics for our future work.

VI. CONCLUSION

In this paper, a radar scheme with raised reflector was described and investigated through the metric of backscattering power to facilitate non-line-of-sight vehicle detection. To this end, a flat rectangular reflector is employed to cast the signal to the blind zone, where a vehicle may be approaching. The proposed scheme shows the best performance, when the reflector's orientation is set as $\alpha = 6°$, $\beta = 45°$, the reflector size is 1.3 m^2 and the reflector's rising height $h = 2.0$ m. Furthermore, C-type radar, due to its wider half-power beamwidths was shown to contribute an additional 5 dB to the backscattering power compared to A-type radar.

In this work, the accurate RCS of the detectable vehicle has been modeled to evaluate the scattering capabilities of the detectable vehicle in the context of the proposed scheme. Although the windshield has a good reflectivity, it cannot effectively be used even for the radar scheme with raised reflector due to windshield's fairly unsuitable slope. Thus, the bumper zone is the most important area for the detection of driving car. The mean RCS magnitude in this zone was shown to be around 2 dBsm, while the standard deviation is 3.4 dB.

In general, the introduction of a precalculated RCS of the passive reflector turned out to be a somewhat problematic task due to the fundamental physical and computational limitations. Therefore, in our future work, we will replace the SBR-based computer simulation of the reflector with an alternative analytical model building on the Kirchhoff approximation.

Finally, it is noted that if the target and the sensing cars are both equipped with radars, operating in the same band, there can be inherent interference challenges complicating the applicability of the proposed scheme. Additional interference mitigation methods should thus be studied and applied which form important topics for future research in this area.

REFERENCES

[1] *Systems Characteristics of Automotive Radars Operating in the Frequency band 76–81 GHz for Intelligent Transport Systems Applications*, document Recommendation ITU-R M.2057-1, 2018.

[2] X. Wang, L. Xu, H. Sun, J. Xin, and N. Zheng, "On-road vehicle detection and tracking using MMW radar and monovision fusion," *IEEE Trans. Intell. Transp. Syst.*, vol. 17, no. 7, pp. 2075–2084, Jul. 2016.

[3] D. Solomitckii, C. B. Barneto, M. Turunen, M. Allen, Y. Koucheryavy, and M. Valkama, "Millimeter-wave automotive radar scheme with passive reflector for blind corner conditions," in *Proc. 14th Eur. Conf. Antennas Propag. (EuCAP)*, Mar. 2020.

[4] E. B. Kamel, A. Peden, and P. Pajusco, "RCS modeling and measurements for automotive radar applications in the W-band," in *Proc. 11th Eur. Conf. Antennas Propag. (EUCAP)*, Mar. 2017, pp. 2445–2449.

[5] S. B. J. Gowdu, A. Schwind, R. Stephan, and M. A. Hein, "Monostatic RCS measurements of a passenger car mock-up at 77 GHz frequency in virtual environment," in *Proc. 49th Eur. Microw. Conf. (EuMC)*, Oct. 2019, pp. 996–999.

[6] Z. Xie, M. Feng, Q. Chen, J. Lin, and Y. Wu, "A research on the electromagnetic scattering of civilian vehicle," in *Proc. Photon. Electromagn. Res. Symp.-Fall (PIERS-Fall)*, Dec. 2019, pp. 2790–2795.

[7] S. Alland, W. Stark, M. Ali, and M. Hegde, "Interference in automotive radar systems: Characteristics, mitigation techniques, and current and future research," *IEEE Signal Process. Mag.*, vol. 36, no. 5, pp. 45–59, Sep. 2019.

[8] J. Rock, M. Toth, E. Messner, P. Meissner, and F. Pernkopf, "Complex signal denoising and interference mitigation for automotive radar using convolutional neural networks," in *Proc. 22nd Int. Conf. Inf. Fusion (FUSION)*. 2019, pp. 1–8.

[9] J. Fuchs, A. Dubey, M. Lübke, R. Weigel, and F. Lurz, "Automotive radar interference mitigation using a convolutional autoencoder," in *Proc. IEEE Int. Radar Conf. (RADAR)*, Apr. 2020, pp. 315–320.

[10] J. Kim, S. Lee, Y.-H. Kim, and S.-C. Kim, "Classification of interference signal for automotive radar systems with convolutional neural network," *IEEE Access*, vol. 8, pp. 176717–176727, 2020.

[11] F. Uysal, "Phase-coded FMCW automotive radar: System design and interference mitigation," *IEEE Trans. Veh. Technol.*, vol. 69, no. 1, pp. 270–281, Jan. 2020.

[12] J. Bechter, F. Roos, M. Rahman, and C. Waldschmidt, "Automotive radar interference mitigation using a sparse sampling approach," in *Proc. Eur. Radar Conf. (EURAD)*, Oct. 2017, pp. 90–93.

[13] Z. Xu and Q. Shi, "Interference mitigation for automotive radar using orthogonal noise waveforms," *IEEE Geosci. Remote Sens. Lett.*, vol. 15, no. 1, pp. 137–141, Jan. 2018.

[14] *Cgtrader Web-Site*. Accessed: Jun. 2020. [Online]. Available: https://www.cgtrader.com/3d-models/car/luxury/mercedes-e-class-exclusive-sedan-hybrid-2017

[15] D. Solomitckii *et al.*, "Characterizing radio wave propagation in urban street canyon with vehicular blockage at 28 GHz," *IEEE Trans. Veh. Technol.*, vol. 69, no. 2, pp. 1227–1236, Feb. 2020.

[16] E. F. Knott, J. F. Schaeffer, and M. T. Tulley, *Radar Cross Section*. Rijeka, Croatia: SciTech, 2004.

[17] M Commens. (Mar. 2018). *Simulating Radar Signatures of Electrically Large Targets in Ansys HFSS*. [Online]. Available: https://www.ansys.com/blog/simulating-radar-signatures-large-targets-ansys-hfss

[18] L. Ansoft, *An Introduction to HFSS Fundamental Principles, Concepts, and Use*, Ansoft, Pittsburgh, PA, USA, 2009, p. 88.

[19] *Effects of Building Materials and Structures on Radiowave Propagation Above About 100 MHz*, document Recommendation ITU-R 2040-1, P Series, 2015.

[20] A. Kilian, J. Weinzierl, and L.-P. Schmidt, "Permittivity measurement techniques at 24 GHz for automotive polymer composites including thin films and paint foils," in *Proc. German Microw. Conf.*, 2008, pp. 1–4.

[21] D. Solomitckii, M. Heino, S. Buddappagari, M. A. Hein, and M. Valkama. (2021). *Dataset of RCS Results Related to NLOS Radar Scheme for Vehicle Detection With Raised Reflector*. [Online]. Available: https://zenodo.org/record/4575994, doi: 10.5281/zenodo.4575994.

[22] C. Aydogdu, M. F. Keskin, N. Garcia, H. Wymeersch, and D. W. Bliss, "RadChat: Spectrum sharing for automotive radar interference mitigation," *IEEE Trans. Intell. Transp. Syst.*, vol. 22, no. 1, pp. 416–429, Jan. 2021.

Mikko Heino (Member, IEEE) received the D.Sc. degree in radio engineering from Aalto University, Helsinki, in 2020. He is currently a Post-Doctoral Research Fellow with the Unit of Electrical Engineering, Tampere University, Finland. His research interests include joint communication and sensing systems, millimeter wave antenna design and user effect characterization, and antenna isolation improvement methods for in-band full-duplex systems.

Sreehari Buddappagari received the B.E. degree in electronics and communication engineering from VTU, Karnataka, in 2011, and the M.Sc. degree in communications and signal processing from Technische Universität Ilmenau, Germany, in 2016, where he is currently pursuing the Ph.D. degree with the RF and Microwave Research Laboratory. Since 2017, he has been working as the Staff Scientist of the RF and Microwave Research Laboratory, TU Ilmenau. His research interests include virtual validation of automotive radar and wireless communication systems, radar cross section measurements and modeling, EM wave propagation, and radar-in-the-loop testing. He also contributes to leadership and management activities in German and international projects.

Matthias A. Hein (Senior Member, IEEE) received the Ph.D. degree from the University of Wuppertal, Germany, where he worked on superconductors for mobile and satellite communications.

In 2002, he joined TU Ilmenau as the Head of the RF and Microwave Research Laboratory. In his professional career, he has co/authored 606 publications and provided more than 60 invited talks, and supervised 43 Ph.D., 93 master's, and 77 undergraduate projects. His research interests include intelligent automotive wireless sensor and communication systems, over-the-air testing, and virtual test drives. His further research deals with antenna and microwave engineering. He is an Elected Board Member of the IEEE Joint German Chapter MTT/AP and further national associations. In 1999, he received the British EPSRC Senior Research Fellowship at the University of Birmingham. He has served as the chair, the co-organizer, and a convener of various international microwave conferences.

Dmitrii Solomitckii received the M.Sc. degree in electronics and microelectronics from St. Petersburg Electrotechnical University "LETI," Russia, in 2008, and the D.Sc. degree in communication engineering from Tampere University, Finland, in 2019. He is currently a Visiting Researcher with the Unit of Electrical Engineering, Tampere University. His research interests include antennas, wave propagation, and PHY signal processing in wireless communication and sensing. He has broad practical experience in designing analogue, digital, and mixed electronic systems for critical applications.

Mikko Valkama (Senior Member, IEEE) received the M.Sc. and D.Sc. degrees (Hons.) from the Tampere University of Technology, Finland, in 2000 and 2001, respectively. He is currently a Full Professor and the Head of the Unit of Electrical Engineering, Tampere University, Finland. His general research interests include radio communications, radio localization, and radio-based sensing, with a particular emphasis on 5G and 6G mobile radio networks.